Stem Cell Reports
Resource
OPEN ACCESS

A Multiwell Cardiac μGMEA Platform for Action Potential Recordings from Human iPSC-Derived Cardiomyocyte Constructs

Stacie L. Edwards,[1] Viviana Zlochiver,[1] Donald B. Conrad,[1] Ravi Vaidyanathan,[2] Andrew M. Valiquette,[3] and Rosy Joshi-Mukherjee[1,4,*]

[1]Aurora Research Institute, Aurora Health Care, 960 N 12th Avenue, Milwaukee, WI 53233, USA
[2]Cellular and Molecular Arrhythmia Research Program, Department of Medicine, Division of Cardiovascular Medicine, University of Wisconsin, Madison, WI 53705, USA
[3]School of Medicine, Creighton University, Omaha, NE 68178, USA
[4]Department of Medicine-Cardiovascular, School of Medicine, Johns Hopkins University; Baltimore, MD 21205, USA
*Correspondence: rosy.joshi-mukherjee@aurora.org
https://doi.org/10.1016/j.stemcr.2018.06.016

SUMMARY

Multielectrode array (MEA) technology has been extensively used for field potential recordings from excitable cells. However, its application for action potential (AP) measurements has not been harnessed. Here, we report a novel platform for high-resolution intracellular AP recordings from induced pluripotent stem cell-cardiomyocyte constructs derived from human cardiac fibroblasts. To gain intracellular access, micro-gold MEAs were used to electroporate multiple constructs simultaneously. High-throughput AP measurements were obtained from 41 multicellular constructs. Repeated electroporations of the same cells did not affect the signal stability. Our model has the capability to distinguish subtle differences in AP morphology to characterize the network profile. Furthermore, we confirm the reliability of the system by recapitulating known drug-induced physiological and arrhythmogenic responses. Overall, the model provides a unique cardio-electronic interface for non-invasive measurements of AP dynamics for drug screening and disease modeling. This technology opens the door for identifying novel cardio-factors to enhance electrophysiological maturation.

INTRODUCTION

Low impedance, multielectrode array (MEA) technology is a well-established method to study electrical conduction by extracellular field potential (FP) measurements from electrogenic cells or tissue (Clements, 2016; Thomas et al., 1972). MEA-based measurements of FPs from a network of induced pluripotent stem cell (iPSC)-derived cardiomyocytes (iPSC-CMs) have recently gained tremendous interest for cardiotoxicity, drug screening, and disease studies (Jans et al., 2017; Strauss et al., 2017; Tertoolen et al., 2018). However, high-throughput electrophysiological recordings of iPSC-CMs to identify dynamic physiological changes due to ion channel mutations, drugs, or aging remains a challenge. In addition, long-term action potential (AP) studies from multicellular preparations are currently lacking, thus limiting our understanding of cardiac physiology in development and in disease. There have been a few reports of intracellular recordings of APs using semiconductor chips and mechanical pressure in *Aplysia* neurons (Cohen et al., 2008), mushroom-shaped MEAs in neurons (Ojovan et al., 2015; Shmoel et al., 2016), iridium oxide nanotube electrodes in neurons and rat HL-1 myocytes (Lin et al., 2014), vertical nanopillar electrodes with HL-1 myocytes (Xie et al., 2012), and complementary metal oxide semiconductor-based MEAs of neonatal rat ventricular myocytes and iPSC-CMs (Braeken et al., 2012; Jans et al., 2017). Although these studies demonstrate the ability of the MEA system to measure APs from excitable cells, these custom-built devices are limited to a few laboratories. Furthermore, studies have lacked in-depth signal analysis to understand the effect of cardiomyocyte maturation on the physiological or drug responses of the network over time.

In this study we developed hiPSC-CM constructs on a multiwell micro-gold MEA (μGMEA) platform capable of long-term electrophysiological recordings. To spearhead the construction of the model, we produced high-purity iPSC-CM cultures from human cardiac fibroblasts. Employing electroporation, we have gained intracellular access to record high-resolution APs from multiple cardiac constructs derived from three independent differentiation batches. With this system we aimed to (1) study dynamic changes in transmembrane potential of hiPSC-CMs in a network, (2) measure and analyze the variability in AP waveforms to examine spatial cardiomyocyte heterogeneity, and (3) accurately modulate AP waveforms and recapitulate cardiac arrhythmogenic responses to drugs. We report intracellular AP measurements from cellular networks using a commercially available MEA system (Multi Channel Systems MCS, Germany). We automated AP analysis to demonstrate the feasibility of the model for long-term studies. Overall, the model will be a valuable tool not only for studying cardiomyocyte development and maturation but also for drug screening and disease modeling.

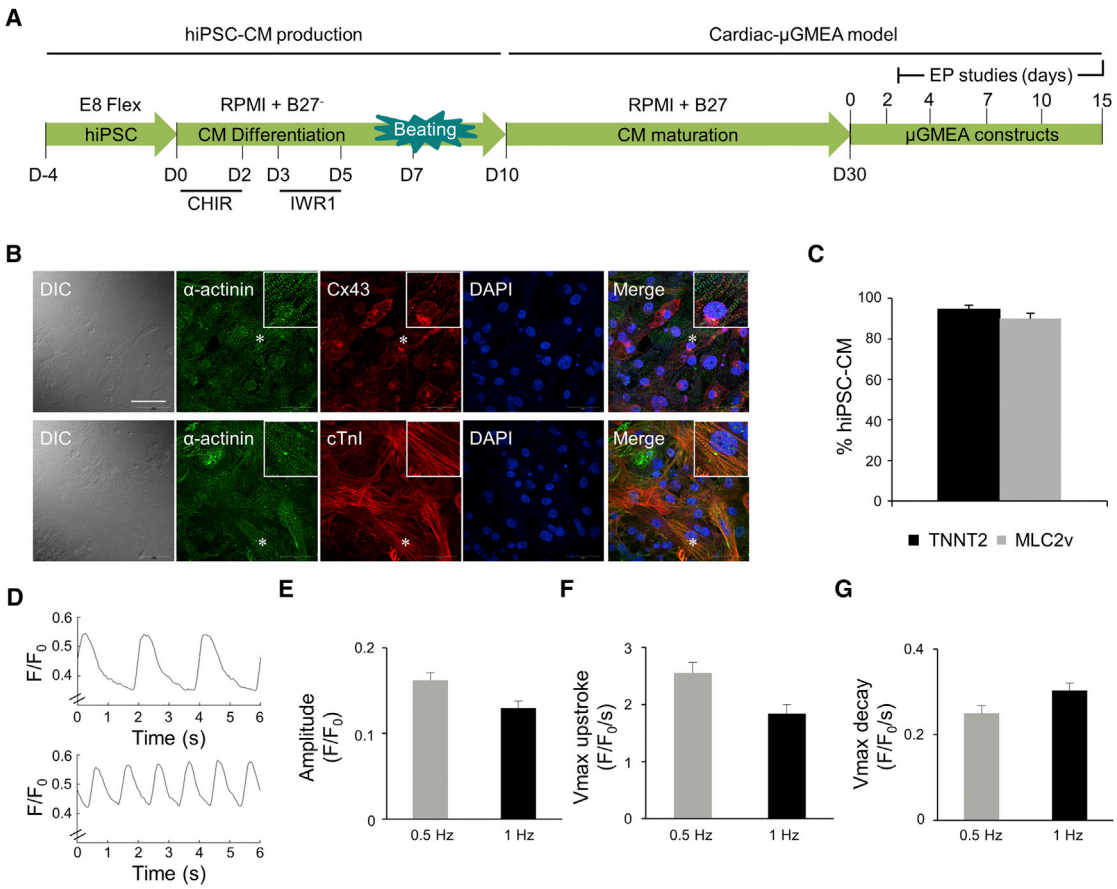

Figure 1. Structural and Functional Maturation of hiPSC-CMs

(A) Timeline of hiPSC cardiomyocyte production and maturation. At day 10 the cardiomyocytes were quality controlled by FACS analysis of TNNT2 and MLC2v and only cultures resulting in >90% cardiomyocytes were cryopreserved for future experiments. hiPSC-CMs were thawed and cultured until day 30 prior to plating on the μGMEA. Electrophysiology (EP) experiments were conducted on 2- to 15-day-old constructs.

(B) Confocal images of α-actinin, Cx43, cTnI, and DAPI nuclear stain in hiPSC-CMs. The inlet shows the zoomed in area marked with an asterisk. Images were taken with 60× objective. Calibration bar represents 50 μm. n = 3 independent experiments. DIC, differential interference contrast.

(C) FACS analysis of TNNT2 and MLC2v. n = 3 independent experiments.

(D) Representative calcium transients (CaTs) at 0.5 Hz (top) and 1 Hz (bottom) using ratiometric Fura-2 dye and IonOptix system.

(E) CaT amplitude.

(F) V_{max} upstroke (maximal departure velocity of the calcium release phase).

(G) V_{max} decay, measurement of the speed of CaT relaxation at 0.5 and 1 Hz.

Data in (B)–(G) were from day 30 hiPSC-CMs. (C) Data expressed as mean ± SEM, n = 3 independent experiments. (D–G) Data at 0.5 and 1 Hz expressed as mean ± SEM, n = 14 technical replicates. See also Figure S1.

RESULTS

Characterization of hiPSC-CMs for the Development of the Cardiac μGMEA Model

Cardiac fibroblast reprogrammed hiPSCs have been reported to efficiently differentiate into cardiomyocytes of high purity (Zhang et al., 2015). In this study we utilized iPSCs reprogrammed from human cardiac fibroblast obtained from a 70-year-old healthy male donor (ATCC). The cell line was examined for stem cell markers OCT-4, SSEA-4, and NANOG (Figure S1A). We optimized the hiPSC feeder free monolayer differentiation protocol as described in Experimental Procedures. Figure 1A depicts the timeline for hiPSC differentiation into cardiomyocytes. Beating cultures at day 10 post differentiation expressed cardiac markers α-actinin, connexin43 (Cx43), and troponin I (cTnI) (Figure S1B). Plating densities of 75,000, 100,000, and 125,000 per 35 mm tissue culture dish produced

>90% cardiomyocytes at day 10 post differentiation as quantified by flow cytometry using cardiac markers MLC2v and TNNT2 (Figure S1C). The plating density of 100,000 cells per well was subsequently selected for hiPSC-CM production. Only cultures of >90% cardiomyocyte purity by fluorescence-activated cell sorting (FACS) analysis of MLC2v and TNNT2 were dissociated at day 10 and cryopreserved for experimental studies. hiPSC-CMs were thawed and cultured until day 30 for cellular and electrophysiological studies (Figure 1A).

α-actinin, cTnI, and Cx43 expression was examined in hiPSC-CMs at day 30 post differentiation by confocal microscopy (Figure 1B) and MLC2v and TNNT2 by flow cytometry (Figure 1C). In contrast to day 10, hiPSC-CMs at day 30 show defined myofilament pattern indicating maturation. Cx43 was localized mainly on the cell membrane with some cell-cell apposition pattern representing gap junctions and intracellular punctate distribution. MLC2v and TNNT2 quantification continued to demonstrate >90% cardiomyocyte purity in day 30 cultures. Overall, we show high-purity hiPSC-CM production with high expression of cardiac markers showing sarcomere and gap-junction organization. The hiPSC-CMs were further examined for functional maturation.

Excitation-contraction coupling is a well-defined cardiomyocyte maturation phenomenon (Bedada et al., 2016; Lundy et al., 2013). The capabilities of our cardiomyocytes to cycle calcium in response to pacing stimuli were tested via the IonOptix system. At day 30, hiPSC-CM calcium transients were visualized using the ratiometric dye Fura-2 (Figure 1D), demonstrating an amplitude drop when the cells were paced at 1 Hz, compared with 0.5 Hz (Figure 1E). Similar trends were observed for their maximal upstroke and decay velocity (Figures 1F and 1G), indicating immature calcium handling. Overall, our monolayer-based differentiation protocol yields high-purity cardiomyocytes with cellular and physiological properties characteristic of an embryonic/neonatal phenotype at day 30 post differentiation.

Cardiac μGMEA Model for Long-Term Electrophysiological Studies

The μGMEA system consists of series of multielectrode arrays each containing 12 micro-gold electrodes embedded on poly-3,4-ethylenedioxythiophene (PEDOT) substrate. Each electrode is 30 μm in diameter with inter-electrode distance of 300 μm. Plating of quality-controlled hiPSC-CMs on each array was optimized to form a syncytial cardiac network. For details on cell plating, see Experimental Procedures. The electrophysiological properties of 41 constructs from three independent differentiation batches were characterized over a period of 15 days (Figure 1A). Spontaneous beating frequencies of the 2- to 15-day-old constructs averaged 36 ± 1 beats/min (BPM) in Figure 2A. FP amplitudes significantly increased over time (Figure 2B) and the signals in 10- and 15-day-old constructs were significantly higher than in earlier time points ($p < 0.0001$ for day 10 and 15). Additionally, the average number of active electrodes per well was 1.8 ± 0.2, 4.4 ± 0.2, 7.5 ± 0.2, 8.3 ± 0.1, and 7.3 ± 0.2 in 2-, 4-, 7-, 10-, and 15-day-old constructs, respectively (averaged across the 41 constructs). The FP amplitudes at day 10 and 15 were not significantly different (<0.8024), thus the 10-day time point was selected for further scrutiny. Average RR intervals and FP durations (FPDs) across the 10-day-old constructs are shown in Figures 2C and 2D, respectively. Representative FP recordings from a 10-day-old μGMEA construct and an average FP waveform with prominent T wave are shown in Figure S2. We tested the viability of the constructs at the end of electrophysiological recordings by phase contrast imaging and immunocytochemistry by epifluorescence imaging to evaluate cellular integrity (Figure S3). The expression of Cx43 was found on the membrane and at cell-cell apposition indicating gap-junction formation. cTnI expression showed a striated pattern indicating myofilament network. Long-term electrophysiological recordings had no detectable detrimental effect on the health of the constructs.

Electroporation-Mediated APs Using μGMEA

Delivery of electroporating pulses to excitable cells allows intracellular access for AP recordings (Hai and Spira, 2012; Xie et al., 2012). The exposure of the cardiac μGMEA constructs to a train of low-voltage pulses (1 V, 1 ms, 1 Hz) for 30 s caused a transient, reversible transformation of FP to AP. Three representative voltage traces of pre-, during, and post-electroporation MEA recordings from three independent constructs are shown in Figure 3A. In the absence of electroporation, the signal recorded was purely FPs. However, in the presence of electroporation, the FP transitioned to quasi-AP within a few seconds, then to complete AP toward the end of electroporation, and then gradually reverted back to FPs. We found that the electroporation effect was local and specific to the electrode where it was applied, as shown by the example in Figure S4A, which shows no perturbation of FP signals from electroporating pulses in the neighboring, non-stimulating electrodes. Similarly, Figure S4B demonstrates APs observed only in the stimulated site post electroporation. Post-electroporation constructs had a mean beating rate of 43 ± 0.4 BPM (Figure S4C). The average unweighted mean amplitude of APs recorded was 13 ± 0.9 mV (Figure S4D) with a signal-to-noise ratio above 68 dB, demonstrating the robustness of the signal. Multiple electroporations of the same cells at 0, 1, 24, and 48 hr had no significant effect on the

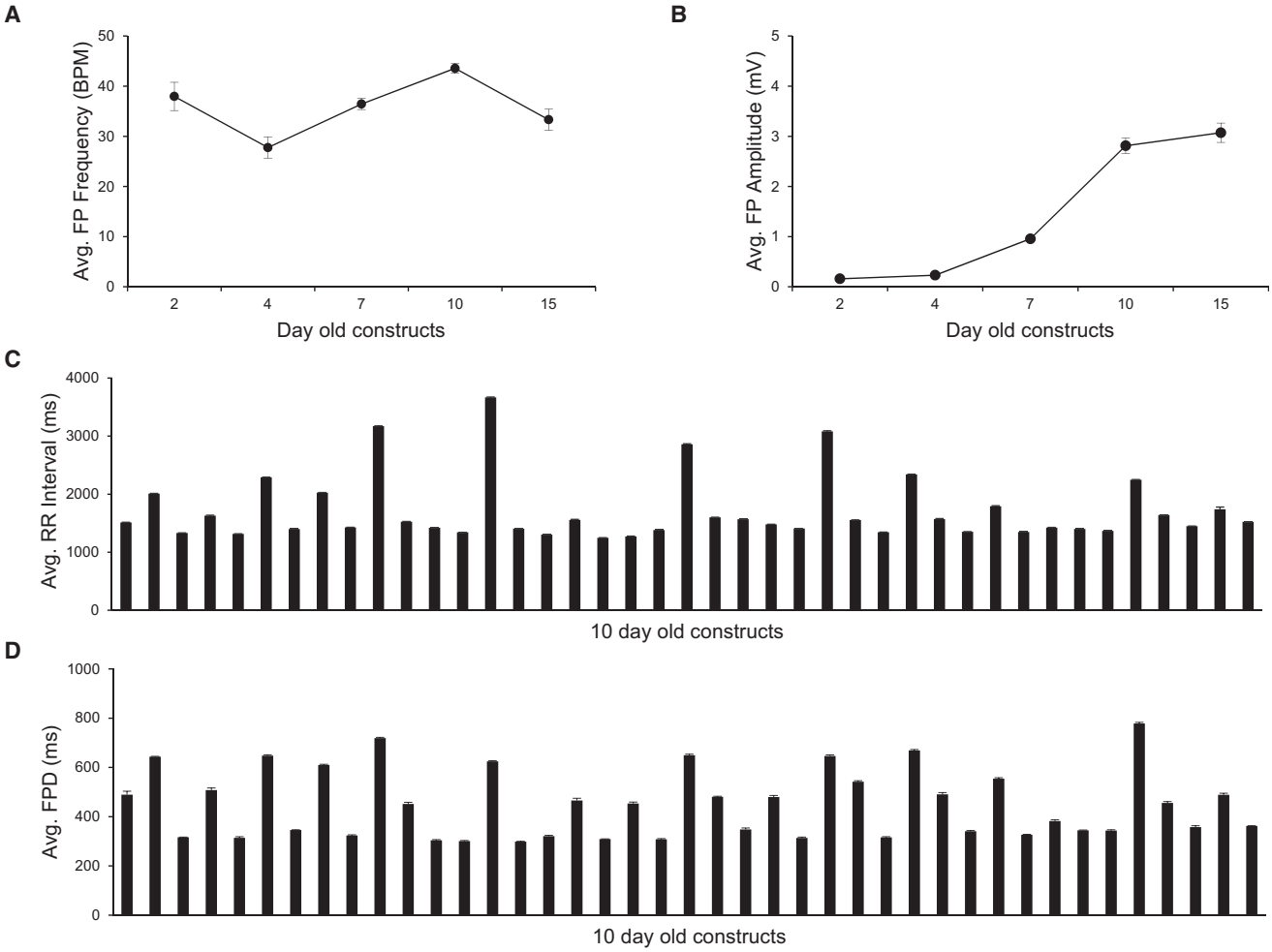

Figure 2. Long-Term Electrophysiological Studies of Cardiac μGMEA Constructs

(A) Average beating frequencies (n = 41 constructs).

(B) Average FP peak-to-peak amplitude. Note a significant increase in the amplitude at day 10 marking electrophysiological maturation (n = 41 constructs).

(C) Average RR interval (n = 341 electrodes).

(D) Average FPD (n = 341 electrodes).

Data expressed as mean ± SEM. Data obtained from three independent batches. See also Figures S2 and S3.

stability and AP shape over time, as shown in Figure 3B, further indicating the repeatability and stability of the model. The reliability of the AP waveform morphology obtained with the μGMEA system was examined by comparing the recordings via MEA and current clamp technique. Waveforms recorded via MEA and patch clamp showed similar AP morphologies (Figure 3C). In order to confirm AP amplitude dependence on the sodium current (I_{Na}) voltage-gated sodium channels were blocked with tetrodotoxin (TTX). Indeed, we observed a dose-dependent attenuation of the AP amplitude and excitability (Figure 3D). Overall, we demonstrate high-amplitude AP measurements that were stable over short and long periods.

AP Heterogeneity within and across Constructs

Optical mapping of beating embryoid bodies (EBs) derived from human embryonic stem cells has recently shown variability of AP durations (Zhu et al., 2016). In order to quantify variability, we implemented a robust MATLAB workflow to rapidly reduce large volumes of raw experimental data into an unbiased grouping of 3,629 AP waveforms recorded from 363 electrodes across 41 constructs (Table S1); for details on signal processing and analysis, refer to Experimental Procedures. The waveforms were analyzed for action potential duration (APD) at various % of repolarization. APD_{30}, APD_{80}, triangulation ($APD_{80} - APD_{30}$), and fractional shortening ($[APD_{80} - APD_{30}]/APD_{80}$) to determine intra- and

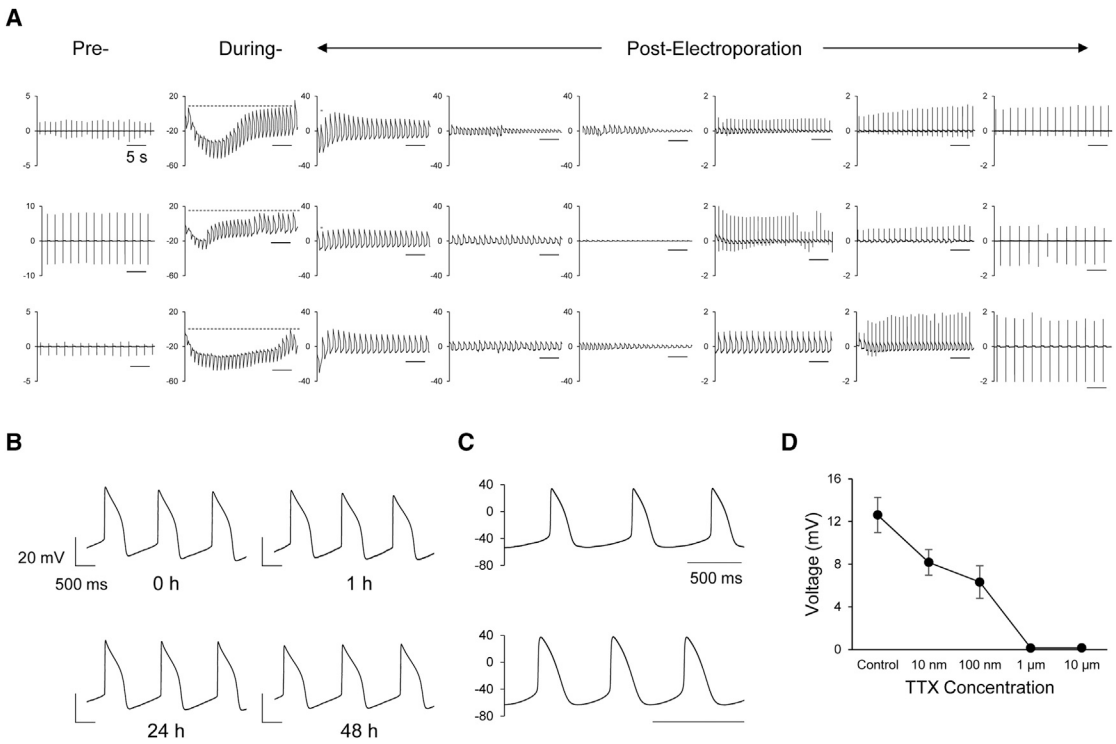

Figure 3. Electroporation-Mediated APs Using μGMEA

(A) Representative pre-, during- and post-electroporation potential recordings from an electrode across three constructs. The scale bar represents 5 s and the y axis represents voltage in mV. AP and FP recordings were obtained at 10 kHz sampling rate.

(B) APs traces obtained from the same cell site over days. Note that multiple electroporation did not affect AP signal quality.

(C) Representative traces of APs recorded from independent constructs using patch clamp. Scale bars represent 500 ms.

(D) TTX response on AP amplitude (n = 11 constructs across three independent batches). Data expressed as mean ± SEM.

See also Figure S4.

inter-construct variability. Figure 4 represents APD_{30} and APD_{80}, whereas Figure 5 shows triangulation and fractional shortening. The distribution of measures from individual waveforms from one batch of differentiation (1,162 waveforms from 13 constructs) is represented in Figures 4A and 5A. The aggregate distribution of mean measurements from all electrodes across a batch, segmented by the three independent batches of differentiation, is displayed in Figures 4B and 5B. The top panels of Figures 4B and 5B highlight that, despite within-construct variability, the distribution of means for all parameters within a batch was well represented by a gaussian distribution fit. Similarly, while intra-batch means varied, overall conformance to gaussian fit persisted across measures and across batches. Quantile correlations for APD_{30}, APD_{80}, triangulation, and fractional shortening were 0.992, 0.989, 0.989, and 0.948, respectively. Furthermore, the coefficient of variation showed general stability across batches for triangulation and fractional shortening, ranging from 0.21 to 0.22 (triangulation) and 0.18 to 0.24 (fractional shortening). Our findings illustrate the importance and utility of having a high-throughput model in order to generate reliable data analysis and meaningful interpretations.

Classification of AP Waveform Morphology

Human cardiomyocytes have been classified into various subtypes based on APD ratio and difference (Kane and Terracciano, 2017). The solid black and dotted lines in Figure 6 represent the reported APD ranges for native human ventricular and atrial subtypes respectively (Drouin et al., 1998; Li et al., 1998; Redpath et al., 2006; Van Wagoner et al., 1999). For comparative purposes, we also segmented the 3,629 AP waveforms based on the APD ratio (APD_{50}/APD_{90}) and the APD difference (APD_{90} − APD_{50}). The plot in Figure 6A shows the data scatter with reference to the native APD ranges. The histograms (insets) show that 90% of the data fall between 0.71 and 0.90 ms and between 44 and 133 ms for APD ratio and difference, respectively. AP waveforms recorded from 302 electrodes fit both criteria. The network properties of 41 clusters were examined for AP morphology using the data between these ranges. The box plots in Figures 6B and 6C highlight the

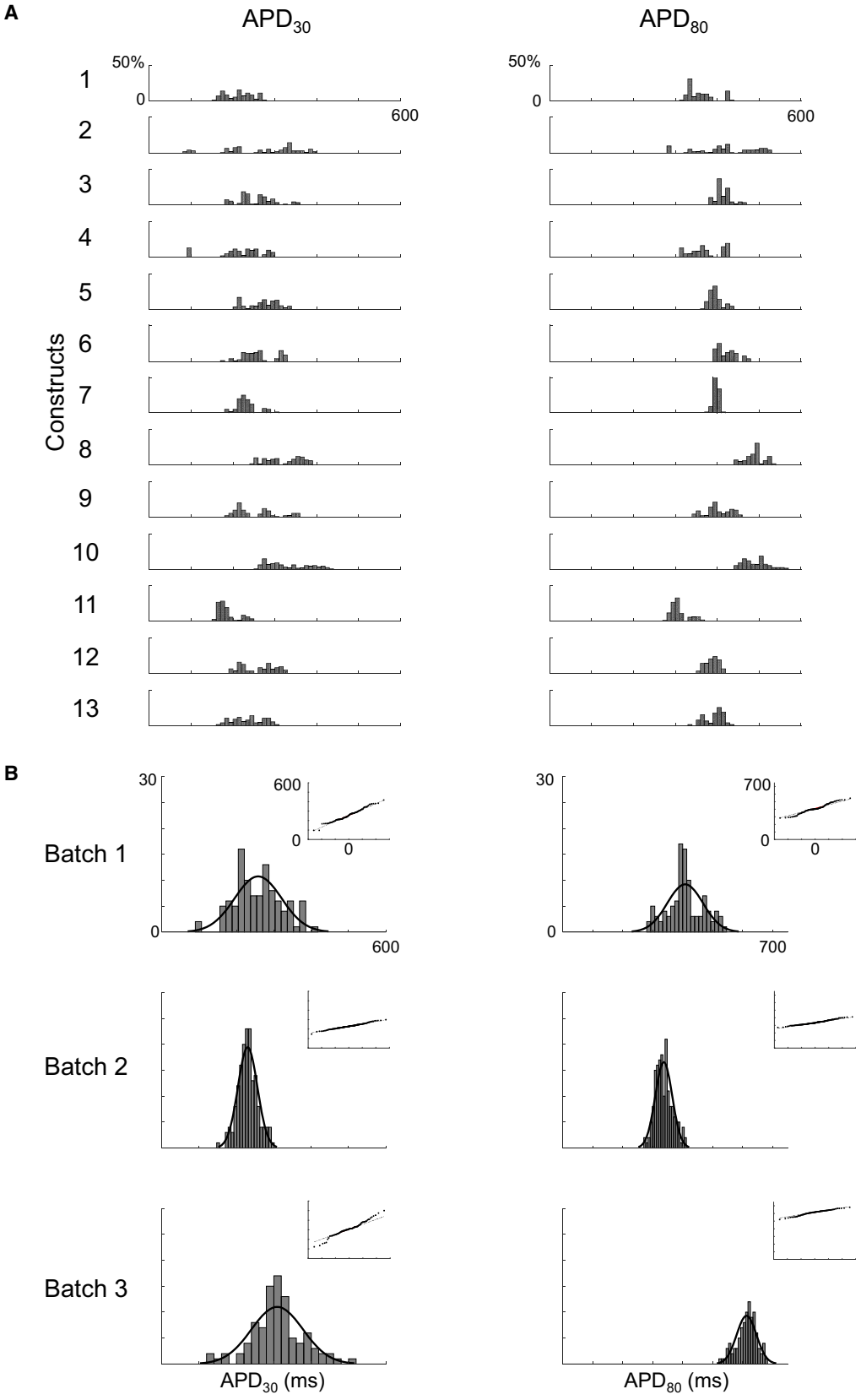

(legend on next page)

interquartile range (box), median (red bar), and maximal dispersion of $APD_{90} - APD_{50}$ and APD_{50}/APD_{90} measurements within and across 41 constructs. "Whiskers" represent ±1.5 times the interquartile range (IQR). Outliers are labeled with a red plus (+) and fall outside of ±1.5 times the IQR. Despite intra-construct variability of median measurements and varying prevalence of outlier observations, overall network properties for the 302 electrode observations meeting both ratio and difference criteria appear to have a ventricular-like profile that is consistent across constructs.

μGMEA Constructs Response to Pharmacological Modulation

β-adrenergic stimulation increases beating frequency and shortens the AP in cardiomyocyte monolayers (Bielawski et al., 2016; Joshi-Mukherjee et al., 2013). When treated with norepinephrine (NE) or isoproterenol (Iso), we observed a dose-dependent increase in beating frequencies (Figures 7A and 7B, left panels). Additionally, shortening of the APD, a characteristic dose-dependent effect of NE and Iso, was also observed. For details on methodology, refer to Experimental Procedures. Overall, average APDs at 10%–90% repolarization show dose-dependent shortening, indicating maturity of the β-adrenergic signaling pathway (Figures 7A and 7B, right panels).

E4031, a known hERG channel blocker, elicited prolongation of the APD and produced arrhythmic early afterdepolarizations (EADs) at higher doses. Also, E4031 showed a dose-dependent reduction in beating frequency as well as a decrease in FP amplitude (Figure 7C, left panels). Furthermore, the average APD_{90} prolongation demonstrates the reliability of the constructs to detect changes in AP dynamics (Figure 7C, right panel). AP data provided a detailed repolarization prolongation response along with EAD occurrences, especially at higher concentrations. Overall, the hiPSC-CM constructs on the μGMEA system not only recapitulated known physiological responses but also reliably detected arrhythmogenicity.

DISCUSSION

iPSC technology provides an unlimited renewable source of cardiomyocytes derived from various donor cell types that have been shown to express ion channels similar to primary human cardiomyocytes (Ebert et al., 2012; Ma et al., 2011; Mordwinkin et al., 2013). We show that cardiac fibroblast reprogrammed hiPSCs when differentiated using the monolayer-based protocol can mature into >90% MLC2v-positive cardiomyocytes at day 10 post differentiation. Additionally, we demonstrate that hiPSC-CMs obtained from multiple independent differentiation batches retain structural and functional properties consistent with embryonic to neonatal phenotype. Derivation of high-purity hiPSC-CMs yielded syncytial monolayers when cultured on a PEDOT-coated μGMEA. Using this model, we show high-fidelity temporal resolution intracellular recordings of APs. Our study validates a high-throughput MEA system for long-term measurements of the APs of cardiac constructs to track their electrical maturation. Furthermore, we provide an extensive data analysis of (1) FPs by extracting parameters such as beating rate, peak-to-peak FP amplitude, FP duration, and RR intervals to determine the maturational plasticity of the constructs across the array; (2) high-temporal-resolution APs in the millivolt range to demonstrate the robustness of the model to visualize the waveforms; and (3) AP morphology based on APD analysis to establish its reliability for cardiac development, drug response, and arrhythmia studies.

Quality-controlled iPSC-CM production is fundamental in developing cardiac models for standardized assays of high predictive value. The monolayer-based differentiation protocol for cardiomyocyte production yielded >90% purity (Figure 1C) at day 30 post differentiation. In addition, 64% hiPSC-CMs expressed the cTnI isoform (data not shown), an adult cardiomyocyte marker (Pioner et al., 2016). Nonetheless, our hiPSC-CMs are still in the early stage of development and are structurally immature (Figure 1B) compared with adult cardiomyocytes. Excitation-contraction coupling studies on hiPSC-CMs at day 30 post differentiation (Figures 1D–1G) suggest that they straddle along the embryonic to neonatal stage as seen in other studies (Lundy et al., 2013; Peinkofer et al., 2016). Cardiac μGMEA electrophysiological data reported in this study also demonstrate electrical maturational plasticity. In the early stages (2–7 days old) the amplitude of the FP signal was significantly lower than those of the later time points (10 and 15 days old) (Figure 2). MEA and hiPSC-CMs are frequently used in combination for drug screening studies (Clements, 2016; Del Alamo et al., 2016; Harris et al., 2013; Navarrete et al., 2013), thus it becomes critical

Figure 4. APD Heterogeneity across Constructs

(A) APD parameter histograms representing intra- and inter-constructs variability in a single batch. APs were examined according to APD_{30} and APD_{80} parameters (total of 1,162 waveforms). y axis represents percentage frequency.

(B) The summation of all histograms per category with gaussian distribution fit from batches 1, 2, and 3. The inlet represents quantile-quantile (Q-Q) plots showing normality.

See also Table S1.

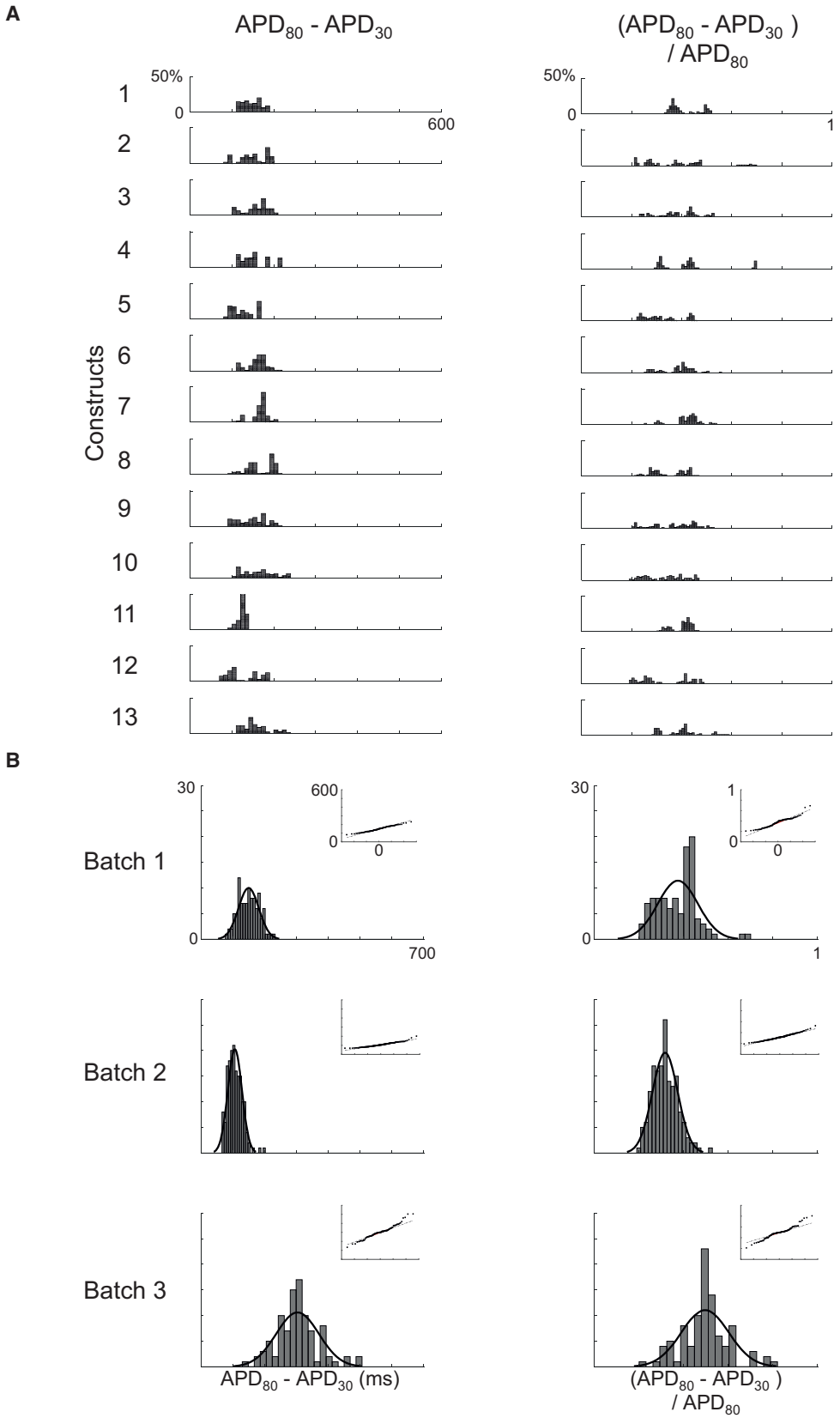

(legend on next page)

to take the electrophysiological maturation of the cells into account when interpreting the results.

Currently, electrophysiological studies using MEA systems provide limited information about APs in multicellular cardiac preparations (Braeken et al., 2012; Jans et al., 2017; Otsuji et al., 2010; Shinozawa et al., 2012). On the other hand, optical mapping of cardiomyocytes in a monolayer has been instrumental in demonstrating the significance of AP shape on cardiac biology, cardiotoxicity, and arrhythmogenesis (Entcheva and Bub, 2016; Joshi-Mukherjee et al., 2013; Zhu et al., 2016). However, they are limited by the quality of the fluorescent signal, spatial resolution of the fluorophore, and cytotoxicity of the dye. Here, we introduce an alternative technique for AP recordings using MEAs that required minimal signal filtering (0.1 Hz high pass and 3,500 Hz low pass filter) (Figures 3, S4, and S5). Application of low-voltage pulse stimulation produced transient reversal of FPs to APs (Figure 3A). The waveforms recorded during 10 s post electroporation across 41 constructs were found to be similar to those recorded from networks of cardiomyocytes by optical mapping (Gorospe et al., 2014; Zhu et al., 2016), complementary metal oxide semiconductor-based MEA (Braeken et al., 2012; Jans et al., 2017), and simulated AP using FP recordings (Tertoolen et al., 2018). Although the current study did not address the mechanism of AP measurement, Hai and Spira (2012) reported in neurons that electropore-electrode interface mimics the established sharp glass microelectrode technique. The post-electroporation transmembrane potential recoveries observed in our study aligns well with the proposed membrane patch mechanisms via Ca^{2+} influx through the injury site reported and discussed previously (Hai and Spira, 2012).

Our μGMEA system allows for monitoring of the APs in the same constructs over time with no signs of detrimental effects on the cellular integrity (Figures 3B and S3). Moreover, multiple permeabilizations of the same cell site over several days did not affect the AP stability. Waveforms recorded via MEA and patch clamp showed similar AP morphologies, indicating that the shape is associated with the intrinsic properties of the membrane rather than changes of access resistance due to permeabilization or resealing (Figures 3B and 3C). The upstroke of the APs recorded via MEA was directly related to the sodium current (I_{Na}), as shown by TTX-mediated voltage-gated sodium channel blockade (Figure 3D). Overall, we demonstrated high-amplitude, I_{Na}-dependent AP measurements that were stable and reliable over short and long periods.

Triangulation and fractional shortening parameters are widely used for drug screening and arrhythmogenesis (Tertoolen et al., 2018; Zhu et al., 2016). Analysis of waveforms at 30% and 80% repolarization along with triangulation and fractional shortening demonstrated AP heterogeneity within and across 41 constructs, indicative of electrophysiological immaturity of cells in the network (Figures 4 and 5). Nonetheless, the conformance of these parameters to a gaussian fit across batches highlights the importance of having a high-throughput system for reliable drug screening and disease modeling.

The percentages of atrial-, nodal-, and ventricular-like subtypes can affect the network properties of cardiomyocyte monolayers (Gorospe et al., 2014; Zhu et al., 2016). Cardiomyocytes derived from iPSCs are a heterogeneous mix of atrial-, nodal-, and ventricular-like cells (Ma et al., 2011; Zhang et al., 2012). APs with similar APD_{30} and APD_{80} can have different morphologies (Gorospe et al., 2014; Zhu et al., 2016). AP shape analysis for difference or ratio of APD_{90} and APD_{50} and comparison with the ranges to those of human ventricular cells with APD_{50}/APD_{90} and $APD_{90} - APD_{50}$ of 0.65–0.85 and 50–130 ms respectively (Kane and Terracciano, 2017) suggests that 90% of the population across all differentiations and constructs were associated with a ventricular-type phenotype (Figure 6). The majority of the waveforms had a longer plateau phase and faster repolarization, representing a ventricular-like morphology (Figures 3B, S4A, S4B, S5B, and S5C). Further studies of chamber-specific gene expression and ion channels by patch clamp are needed to refine cardiomyocyte subpopulation in our model.

The comprehensive *in vitro* proarrhythmia assay initiative recommends the use of multielectrode arrays and hiPSC-CMs for preclinical screening of drugs for cardiotoxicity, QT prolongation, and arrhythmogenic risk (Strauss and Blinova, 2017; Tertoolen et al., 2018). Our cardiac μGMEA model shows a dose-dependent effect of NE and Iso associated with fight-or-flight response (Tank and Lee Wong, 2015) and β-adrenergic (Campbell et al., 2014) stimulation on increase in beating rate and shortening of both FPD and APD (Figures 7A and 7B), thus recapitulating cardiac physiological responses as reported earlier (He et al., 2003; Navarrete et al., 2013). E4031, a hERG channel blocker, elicited dose-dependent prolongation of the APD and produced arrhythmic early afterdepolarizations (EADs) at higher doses, thus modulating AP waveforms via external factors (Figure 7C).

Figure 5. Triangulation and Fractional Shortening

(A) Triangulation ($APD_{80} - APD_{30}$) and fractional shortening ($APD_{80} - APD_{30}/APD_{80}$) histograms using the data in Figure 4A.
(B) The summation of all histograms per category as described in Figure 4B.
See also Table S1.

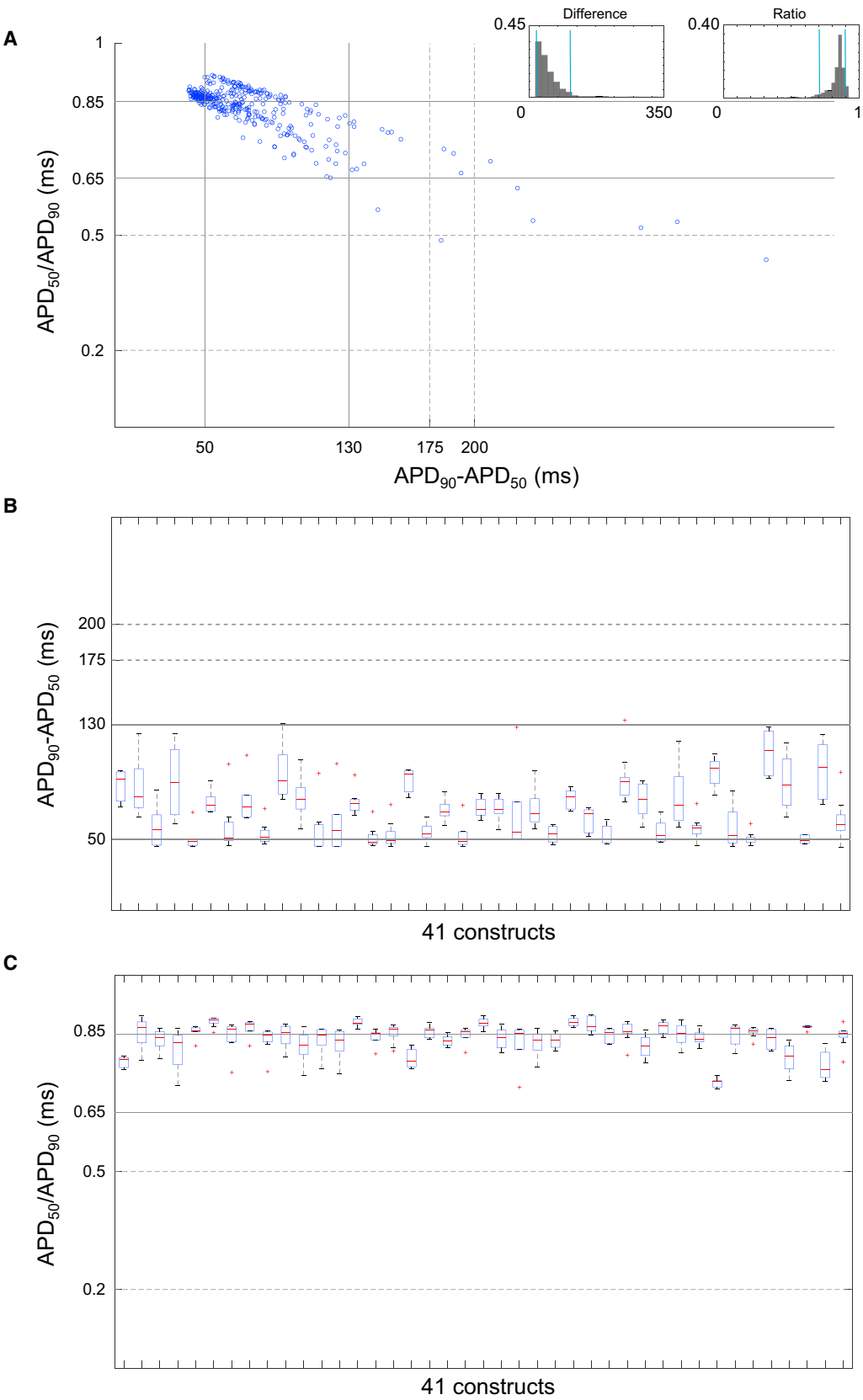

(legend on next page)

Overall, we demonstrate that the model shows consistent electrophysiological properties compared with embryonic stem cell-derived beating EB models (Gorospe et al., 2014; Zhu et al., 2016). Our model has the capability to distinguish subtle differences in AP morphology. Together with the possibility of recording long term from the same construct, this technology opens the door for identifying novel cardio-factors to enhance electrophysiological maturation. The advantages of our high-throughput cardiac μGMEA model, unlike other custom-built devices available to few laboratories, are (1) it allows for non-invasive electrophysiological studies from multiple independent monolayer constructs; (2) it is a high-fidelity powerful tool for long-term effect of ion channels, signaling molecules, and gene expression on the AP; (3) it overcomes the limitation of single use, one at a time monolayer studies that could yield misleading results due to short-term electrophysiological effects; (4) studying AP dynamics of cardiomyocyte development in a network will greatly enhance our understanding of cardiac physiology.

We conclude that the cardiac μGMEA model presents a unique cardio-electronic interface that allows high-fidelity measurements of APs for cardiomyocyte development and maturation studies. It is a high-throughput platform for screening novel cardio-factors. Effect of diseases or mutations on cardiac development and maturation could easily be conducted on the same cells for an extended period of time. Furthermore, membrane rupture and repair are of clinical significance in age-associated cardiomyopathies and thus subtle changes in APs over a period of time might have implications on cardiomyocyte pathophysiology. Overall, the study demonstrates that non-invasive long-term AP measurement and modulation will advance our understanding of cardiac biology and arrhythmia.

EXPERIMENTAL PROCEDURES

hiPSC Cell Culture and Cardiomyocyte Differentiation

An iPSC line derived from human cardiac fibroblasts was purchased from ATCC (ACS-1021). We optimized the feeder free monolayer differentiation protocol as previously described (Bhattacharya et al., 2014). Briefly, the hiPSCs were plated on Geltrex (A1413202, Thermo Fisher)-coated six-well tissue culture dishes and cultured in Essential 8 Flex medium. For cardiomyocyte differentiation, hiPSCs were plated at a density of 100,000 cells/well, coated with Geltrex, and cultured in Essential 8 medium supplemented with Rho Kinase inhibitor, Y-27632 (1254, R&D Systems). After 24 hr the Rho Kinase inhibitor was removed and the cells were cultured for 4 days (Figure 1A). On day 0, the cultures were initiated for differentiation using RPMI with B27 minus insulin (CM differentiation media) containing 6 μM CHIR99021 (4423, R&D Systems) for 48 hr. On day 3, the cultures were treated with 5 μM IWR-1 (I0161, Sigma Aldrich) for 48 hr. Subsequently, the cultures were maintained in cardiomyocyte differentiation media until day 10. Spontaneously beating cultures were observed around day 7 and hiPSC-CMs were cryopreserved at day 10.

Cardiac μGMEA Constructs and MEA Recording

PEDOT-coated 24-well micro-gold multielectrode array (μGMEA) dishes (catalog number 24W300/30G-288, Multi Channel Systems MCS, Germany) contained an array of 12 electrodes per well. Prior to cell plating on the array, a cryovial of 2 million to 3 million hiPSC-CMs frozen at 10 days post differentiation was thawed and 800,000 cells/well were plated in a six-well tissue culture dish coated with Geltrex. Medium was replaced every 2–3 days with fresh RPMI with B27 supplement for 20 days to attain maturity. After a 30-min hydrophilic treatment with fetal bovine serum (FBS), the wells were coated with fibronectin (50 μg/mL) for 3 hr at 37°C. On day 30 the hiPSC-CMs cultures were dissociated using Accutase (Sigma, catalog number A6964) enzyme and plated at 30,000 cells/5 μL/μGMEA well. At this point the cultures are referred to as 0-day-old construct (Figure 1A). Spontaneous beating of cardiomyocytes was first observed in 2-day-old constructs.

FPs were recorded from 2- to 15-day-old constructs and APs from 10-day-old constructs at a sampling rate of 20 kHz unless otherwise noted. FPs of <100 μV and APs of <1 mV were excluded from the analysis. For experiments where electrodes were stimulated, an electroporating pulse (1 V, 1 Hz, and 1 ms) was delivered for 30 s. High- and low-pass filters of 0.1 Hz and 3500 Hz respectively were used for data acquisition. NE, Iso, E4031, and TTX were incubated for 2 min prior to FP and AP recordings.

Patch Clamp Recording of the Construct for APs

Cardiac APs were recorded from cardiomyocyte networks plated according to MEA plating at 30,000 cells/5 μL/coverslip. Glass coverslips were coated with fibronectin (50 μg/mL) for 3 hr at 37°C. hiPSC-CM thawing and plating was carried out similar to

Figure 6. Classification of AP Waveform Morphology

(A) AP waveform distribution from 363 electrodes across 41 constructs based on APD_{50}/APD_{90} and $APD_{50} - APD_{90}$. APD difference and ratio histograms in the left and right insets represent the data in the scatterplot where the blue lines indicate the ranges containing 90% of the values (302 electrodes).

(B and C) $APD_{90} - APD_{50}$ and APD_{50}/APD_{90} plots, respectively, to show the overall network composition of the constructs across the array. The box plots display the interquartile range (box), median (red bar), and whiskers represent the ±1.5 times the interquartile range (IQR). Outliers are labeled with a red plus (+). N = 302 electrodes.

The solid and dotted line ranges represent ventricle and atrial AP phenotype of adult cardiomyocytes, respectively. Data obtained from three independent batches. See also Table S1.

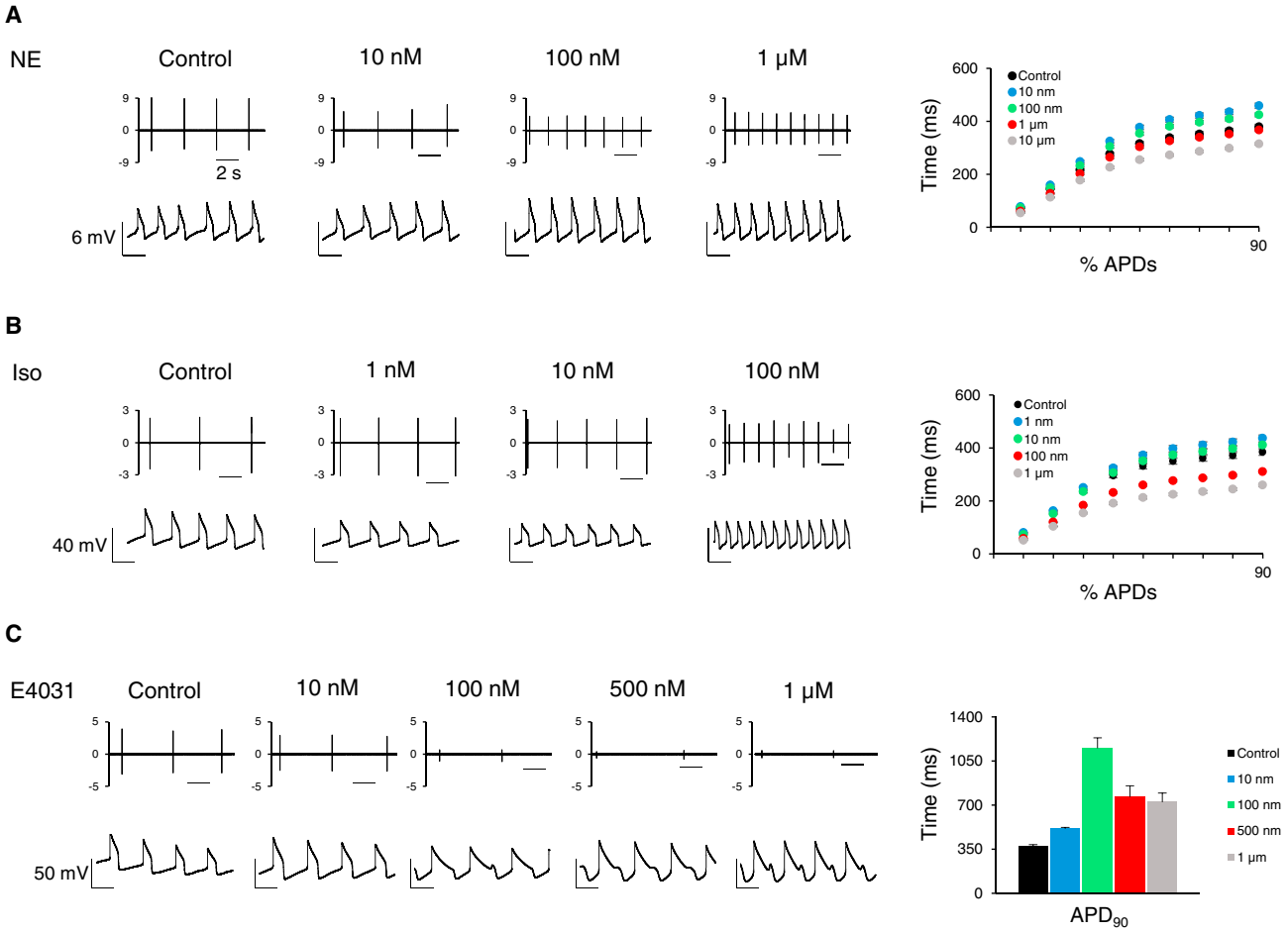

Figure 7. μGMEA Construct Response to Pharmacological Modulation

(A) NE response on FPs (top) and APs (bottom). Right panel, average t-estimates (milliseconds) of percentage APDs at different doses. N = 7 constructs.

(B) Same as above for Iso. N = 8 constructs.

(C) E4031 response on FP (top) and AP (bottom). Note the EADs elicited by 100 nM and above. Right panel, average t-estimates (milliseconds) of APD_{90} at different doses. N = 9 constructs.

Data expressed as mean ± SEM. Data obtained from three independent batches. The scale bar represents 2 s.

the MEA plating described earlier. The constructs were cultured for an additional 10 days for maturation and subjected to patch clamp studies. The glass coverslips containing the constructs were perfused with extracellular solution containing (in mM) NaCl, 148; KCl, 5.4; $CaCl_2$, 1.8; $MgCl_2$, 1; NaH_2PO_4, 0.4; glucose, 5.5; HEPES (4-(2-hydroxyethyl)-1-piperazineethanesulfonic acid), 15, pH was adjusted to 7.4 by NaOH, at 37°C. Pipettes were pulled from thick-walled borosilicate glass capillaries with a Flaming/Brown micropipette puller (P-97) (Sutter Instrument, Novato, CA) and had pipette resistances between 5 and 7 MΩ when filled with intracellular solution containing (in mM) KCl, 150; NaCl, 5; $CaCl_2$, 2; EGTA (ethylene glycol-bis(β-aminoethyl ether)-N,N,N′,N′-tetraacetic acid), 5; HEPES, 10; MgATP, 5 (pH adjusted to 7.2 by KOH). Spontaneous APs were recorded under current clamp mode at 32°C and data were acquired at 10 kHz and filtered at 5 kHz with the Axopatch 200B patch clamp amplifier and pClamp10.0 software (Molecular Devices, Sunnyvale, CA). Spontaneous APs were recorded under current clamp mode as described previously (Vaidyanathan et al., 2016).

Immunocytochemistry

Immunocytochemistry of hiPSCs (Figure S1), hiPSC-CMs (Figures 1 and S1), and cardiac μGMEA constructs (Figure S3) was performed according to a previously established protocol (Joshi-Mukherjee et al., 2013). For details on buffers and antibodies, refer to Table S2. DAPI (1:100, Invitrogen) was used as a nuclear counterstain. Blocking solution was 5% non-fat milk in Dulbecco's PBS (D-PBS). hiPSCs and hiPSC-CMs were mounted with ProLong Gold Antifade Mountant and visualized using a confocal microscope (Olympus IX83 microscope, Fluoview Ver 4.2a software). Cardiac μGMEA constructs stained for Troponin I and Cx43 were visualized using EVOS FL Cell Imaging System.

Flow Cytometry

Flow cytometry was performed on day 10 and day 30 post-differentiated hiPSC-CMs. The cells were washed with D-PBS and dissociated using Accutase for 4 min at 37°C. Cells were centrifuged at 200 × *g* for 5 min at 4°C. The remainder of the procedure was performed on ice. Cells were re-suspended in cell wash solution (1% FBS in D-PBS) and >100,000 cells per experiment were fixed for 15 min and washed once with cell wash solution. Cells were permeabilized for 30 min followed by two washes and then blocked in 100 μL of blocking solution (10% goat serum in 1% PBS) for 25 min. See Table S2 for respective buffers for each antibody. Primary antibodies were added directly to the flow cytometry tubes and were incubated for 45 min with gentle rocking. Cells were washed once with cell wash solution and then re-suspended in 100 μL of blocking solution. The cells were incubated in secondary antibodies for 30 min with gentle rocking in the dark. Cells were then washed twice with cell wash solution and then re-suspended in 400 μL of cell maintenance solution (5% FBS in Hank's balanced salt solution without Ca^{2+} and Mg^{2+}). Data were collected on the BD LSR Fortessa and analyzed using FACSDiva v8.0.1. Gating parameters were defined using cells incubated with only the secondary antibody. For details on primary and secondary antibodies see Table S2.

Calcium Transient Measurement

Total intracellular calcium ($[Ca^{2+}]_i$) was determined using Fura-2/AM (Molecular Probes) according to our protocol described in Joshi-Mukherjee et al. (2013). Briefly, the hiPSC-CMs were loaded with Fura-2/AM (2.5 μM) for 30 min at room temperature. The cells were washed in Tyrode solution for 10 min to remove excess dye and allow for de-esterification. Electrical pacing of the cells was done via IonOptix MyoPacer at 9 V and a frequency of 0, 0.5, or 1.0 Hz. IonOptix equipment (Xenon arc lamp, fluorescence hyperswitch, MyoCam, and a photomultiplier tube) was used to measure 510 nm fluorescence after excitation at alternating wavelengths of 340 and 380 nm. The 340/380 nm fluorescence ratio was used as an indicator of $[Ca^{2+}]_i$.

Signal Processing and Data Analysis

MEA data were acquired using the Multiwell-Screen software, and FP data were analyzed using the Multiwell-Analyzer software (Multi Channel Systems MCS). For AP analysis, data were converted using MCS' Multi Channel DataManager software into HDF5 (.h5) Hierarchical Data Format (HDF) and imported into MATLAB (MathWorks) using the McsHDF5 MATLAB toolbox (also developed by MCS). A custom MATLAB graphical user interface (GUI) and code was combined with MATLAB Signal Processing and Statistics and Machine Learning Toolboxes to produce a signal extraction, quality assurance, and segmentation workflow. Electroporation time points were overlaid with signal to automatically segment and extract 10 s of AP data post electroporation. The GUI allowed for adjustments to the extraction window in the event of a significant deviation or delay in the observed response. The selected window was forwarded to subroutines for automated peak segmentation, rescaling, and analysis (example of extraction of AP data from four sequential electrodes highlighted by red boxes shown in Figure S5A). Each of 3,629 AP waveforms from 363 electrode recordings was segmented by detecting the peaks of the inverse data signal; i.e., the lowest point between each respective AP waveform. The resulting vectors of individual waveforms were then normalized to their respective amplitude (non-dimensional y axis range of 0–1 for all waveforms) and its time vector normalized to the experimental time where the respective AP peak was found within the segmented window (x axis center at 0 for all peaks). Subsequent interpolation of intersection points along the rescaled waveforms was used to generate APD measurements for each of the 3,629 waveforms. Individual waveform calculations were used to determine AP variability within and across the constructs (Figures 4, 5, 6B, and 6C). The classification of AP waveforms shown in Figure 6A and distribution of measurements across differentiated batches in Figures 4B and 5B were performed by superimposing all the AP waveforms within each of the 363 electrodes to find an average measurement (Figures S5B and S5C showing pre and post segmentation, normalization, and superimposition, respectively).

SUPPLEMENTAL INFORMATION

Supplemental Information includes five figures and two tables and can be found with this article online at https://doi.org/10.1016/j.stemcr.2018.06.016.

AUTHOR CONTRIBUTIONS

R.J.-M. conceived the project, designed the experiments, and wrote the manuscript. S.L.E., V.Z., and R.J.-M. performed hiPSC cell culture and differentiation into cardiomyocytes, flow cytometry, immunocytochemistry, and MEA studies to record FPs and APs. A.M.V. and R.J.-M. conducted and optimized calcium transient experiments. R.V. performed the patch clamp experiments. D.B.C. developed the MATLAB script for MEA data extraction and automation for AP analysis.

ACKNOWLEDGMENTS

We thank Dr. Gordon Tomaselli (Johns Hopkins University) for helpful discussion and feedback. The late Dr. Thomas Meyer (Multi Channel Systems MCS, Germany) provided suggestions on cell plating and FP and AP recordings that were extremely valuable in conducting the experiments. We thank Sean Ryan (Research Associate) for confocal imaging of the hiPSCs and hiPSC-CMs and Dr. John Richards for flow cytometry experiments. Manoj Khanal (University of Wisconsin, Milwaukee) and Elizabeth Moenck (Milwaukee School of Engineering) helped in developing the MATLAB script for MEA data extraction and automation. This work was supported by the Aurora Research Foundation and the Cardiovascular Surgery Research Award (CVSRA) (to R.J.-M.).

Received: December 5, 2017
Revised: June 20, 2018
Accepted: June 21, 2018
Published: July 19, 2018

REFERENCES

Bedada, F.B., Wheelwright, M., and Metzger, J.M. (2016). Maturation status of sarcomere structure and function in human iPSC-derived cardiac myocytes. Biochim. Biophys. Acta *1863*, 1829–1838.

Bhattacharya, S., Burridge, P.W., Kropp, E.M., Chuppa, S.L., Kwok, W.M., Wu, J.C., Boheler, K.R., and Gundry, R.L. (2014). High efficiency differentiation of human pluripotent stem cells to cardiomyocytes and characterization by flow cytometry. J. Vis. Exp., 52010. https://doi.org/10.3791/52010.

Bielawski, K.S., Leonard, A., Bhandari, S., Murry, C.E., and Sniadecki, N.J. (2016). Real-time force and frequency analysis of engineered human heart tissue derived from induced pluripotent stem cells using magnetic sensing. Tissue Eng. Part C Methods *22*, 932–940.

Braeken, D., Jans, D., Huys, R., Stassen, A., Collaert, N., Hoffman, L., Eberle, W., Peumans, P., and Callewaert, G. (2012). Open-cell recording of action potentials using active electrode arrays. Lab Chip *12*, 4397–4402.

Campbell, A.S., Johnstone, S.R., Baillie, G.S., and Smith, G. (2014). β-Adrenergic modulation of myocardial conduction velocity: connexins vs. sodium current. J. Mol. Cell. Cardiol. *77*, 147–154.

Clements, M. (2016). Multielectrode array (MEA) assay for profiling electrophysiological drug effects in human stem cell-derived cardiomyocytes. Curr. Protoc. Toxicol. *68*, 22.4.1–22.4.32.

Cohen, A., Shappir, J., Yitzchaik, S., and Spira, M.E. (2008). Reversible transition of extracellular field potential recordings to intracellular recordings of action potentials generated by neurons grown on transistors. Biosens. Bioelectron. *23*, 811–819.

Del Alamo, J.C., Lemons, D., Serrano, R., Savchenko, A., Cerignoli, F., Bodmer, R., and Mercola, M. (2016). High throughput physiological screening of iPSC-derived cardiomyocytes for drug development. Biochim. Biophys. Acta *1863*, 1717–1727.

Drouin, E., Lande, G., and Charpentier, F. (1998). Amiodarone reduces transmural heterogeneity of repolarization in the human heart. J. Am. Coll. Cardiol. *32*, 1063–1067.

Ebert, A.D., Liang, P., and Wu, J.C. (2012). Induced pluripotent stem cells as a disease modeling and drug screening platform. J. Cardiovasc. Pharmacol. *60*, 408–416.

Entcheva, E., and Bub, G. (2016). All-optical control of cardiac excitation: combined high-resolution optogenetic actuation and optical mapping. J. Physiol. *594*, 2503–2510.

Gorospe, G., Zhu, R., Millrod, M.A., Zambidis, E.T., Tung, L., and Vidal, R. (2014). Automated grouping of action potentials of human embryonic stem cell-derived cardiomyocytes. IEEE Trans. Biomed. Eng. *61*, 2389–2395.

Hai, A., and Spira, M.E. (2012). On-chip electroporation, membrane repair dynamics and transient in-cell recordings by arrays of gold mushroom-shaped microelectrodes. Lab Chip *12*, 2865–2873.

Harris, K., Aylott, M., Cui, Y., Louttit, J.B., McMahon, N.C., and Sridhar, A. (2013). Comparison of electrophysiological data from human-induced pluripotent stem cell-derived cardiomyocytes to functional preclinical safety assays. Toxicol. Sci. *134*, 412–426.

He, J.Q., Ma, Y., Lee, Y., Thomson, J.A., and Kamp, T.J. (2003). Human embryonic stem cells develop into multiple types of cardiac myocytes: action potential characterization. Circ. Res. *93*, 32–39.

Jans, D., Callewaert, G., Krylychkina, O., Hoffman, L., Gullo, F., Prodanov, D., and Braeken, D. (2017). Action potential-based MEA platform for in vitro screening of drug-induced cardiotoxicity using human iPSCs and rat neonatal myocytes. J. Pharmacol. Toxicol. Methods *87*, 48–52.

Joshi-Mukherjee, R., Dick, I.E., Liu, T., O'Rourke, B., Yue, D.T., and Tung, L. (2013). Structural and functional plasticity in long-term cultures of adult ventricular myocytes. J. Mol. Cell. Cardiol. *65*, 76–87.

Kane, C., and Terracciano, C.M.N. (2017). Concise review: Criteria for chamber-specific categorization of human cardiac myocytes derived from pluripotent stem cells. Stem Cells *35*, 1881–1897.

Li, G.R., Feng, J., Yue, L., and Carrier, M. (1998). Transmural heterogeneity of action potentials and Ito1 in myocytes isolated from the human right ventricle. Am. J. Physiol. *275*, H369–H377.

Lin, Z.C., Xie, C., Osakada, Y., Cui, Y., and Cui, B. (2014). Iridium oxide nanotube electrodes for sensitive and prolonged intracellular measurement of action potentials. Nat. Commun. *5*, 3206.

Lundy, S.D., Zhu, W.Z., Regnier, M., and Laflamme, M.A. (2013). Structural and functional maturation of cardiomyocytes derived from human pluripotent stem cells. Stem Cells Dev. *22*, 1991–2002.

Ma, J., Guo, L., Fiene, S.J., Anson, B.D., Thomson, J.A., Kamp, T.J., Kolaja, K.L., Swanson, B.J., and January, C.T. (2011). High purity human-induced pluripotent stem cell-derived cardiomyocytes: electrophysiological properties of action potentials and ionic currents. Am. J. Physiol. Heart Circ. Physiol. *301*, H2006–H2017.

Mordwinkin, N.M., Burridge, P.W., and Wu, J.C. (2013). A review of human pluripotent stem cell-derived cardiomyocytes for high-throughput drug discovery, cardiotoxicity screening, and publication standards. J. Cardiovasc. Transl. Res. *6*, 22–30.

Navarrete, E.G., Liang, P., Lan, F., Sanchez-Freire, V., Simmons, C., Gong, T., Sharma, A., Burridge, P.W., Patlolla, B., Lee, A.S., et al. (2013). Screening drug-induced arrhythmia [corrected] using human induced pluripotent stem cell-derived cardiomyocytes and low-impedance microelectrode arrays. Circulation *128*, S3–S13.

Ojovan, S.M., Rabieh, N., Shmoel, N., Erez, H., Maydan, E., Cohen, A., and Spira, M.E. (2015). A feasibility study of multi-site, intracellular recordings from mammalian neurons by extracellular gold mushroom-shaped microelectrodes. Sci. Rep. *5*, 14100.

Otsuji, T.G., Minami, I., Kurose, Y., Yamauchi, K., Tada, M., and Nakatsuji, N. (2010). Progressive maturation in contracting cardiomyocytes derived from human embryonic stem cells: qualitative effects on electrophysiological responses to drugs. Stem Cell Res. *4*, 201–213.

Peinkofer, G., Burkert, K., Urban, K., Krausgrill, B., Hescheler, J., Saric, T., and Halbach, M. (2016). From early embryonic to adult stage: comparative study of action potentials of native and pluripotent stem cell-derived cardiomyocytes. Stem Cells Dev. *25*, 1397–1406.

Pioner, J.M., Racca, A.W., Klaiman, J.M., Yang, K.C., Guan, X., Pabon, L., Muskheli, V., Zaunbrecher, R., Macadangdang, J., Jeong, M.Y., et al. (2016). Isolation and mechanical measurements of myofibrils from human induced pluripotent stem cell-derived cardiomyocytes. Stem Cell Reports *6*, 885–896.

Redpath, C.J., Rankin, A.C., Kane, K.A., and Workman, A.J. (2006). Anti-adrenergic effects of endothelin on human atrial action potentials are potentially anti-arrhythmic. J. Mol. Cell. Cardiol. *40*, 717–724.

Shinozawa, T., Imahashi, K., Sawada, H., Furukawa, H., and Takami, K. (2012). Determination of appropriate stage of human-induced pluripotent stem cell-derived cardiomyocytes for drug screening and pharmacological evaluation in vitro. J. Biomol. Screen. *17*, 1192–1203.

Shmoel, N., Rabieh, N., Ojovan, S.M., Erez, H., Maydan, E., and Spira, M.E. (2016). Multisite electrophysiological recordings by self-assembled loose-patch-like junctions between cultured hippocampal neurons and mushroom-shaped microelectrodes. Sci. Rep. *6*, 27110.

Strauss, D.G., and Blinova, K. (2017). Clinical trials in a dish. Trends Pharmacol. Sci. *38*, 4–7.

Strauss, D.G., Vicente, J., Johannesen, L., Blinova, K., Mason, J.W., Weeke, P., Behr, E.R., Roden, D.M., Woosley, R., Kosova, G., et al. (2017). A common genetic variant risk score is associated with drug-induced QT prolongation and Torsade de pointes risk: a pilot study. Circulation *135*, 1300–1310.

Tank, A.W., and Lee Wong, D. (2015). Peripheral and central effects of circulating catecholamines. Compr. Physiol. *5*, 1–15.

Tertoolen, L.G., Braam, S.R., van Meer, B.J., Passier, R., and Mummery, C.L. (2018). Interpretation of field potentials measured on a multi electrode array in pharmacological toxicity screening on primary and human pluripotent stem cell-derived cardiomyocytes. Biochem. Biophys. Res. Commun. *497*, 1135–1141.

Thomas, C.A., Jr., Springer, P.A., Loeb, G.E., Berwald-Netter, Y., and Okun, L.M. (1972). A miniature microelectrode array to monitor the bioelectric activity of cultured cells. Exp. Cell Res. *74*, 61–66.

Vaidyanathan, R., Markandeya, Y.S., Kamp, T.J., Makielski, J.C., January, C.T., and Eckhardt, L.L. (2016). IK1-enhanced human-induced pluripotent stem cell-derived cardiomyocytes: an improved cardiomyocyte model to investigate inherited arrhythmia syndromes. Am. J. Physiol. Heart Circ. Physiol. *310*, H1611–H1621.

Van Wagoner, D.R., Pond, A.L., Lamorgese, M., Rossie, S.S., McCarthy, P.M., and Nerbonne, J.M. (1999). Atrial L-type Ca2+ currents and human atrial fibrillation. Circ. Res. *85*, 428–436.

Xie, C., Lin, Z., Hanson, L., Cui, Y., and Cui, B. (2012). Intracellular recording of action potentials by nanopillar electroporation. Nat. Nanotechnol. *7*, 185–190.

Zhang, J., Klos, M., Wilson, G.F., Herman, A.M., Lian, X., Raval, K.K., Barron, M.R., Hou, L., Soerens, A.G., Yu, J., et al. (2012). Extracellular matrix promotes highly efficient cardiac differentiation of human pluripotent stem cells: the matrix sandwich method. Circ. Res. *111*, 1125–1136.

Zhang, L., Guo, J., Zhang, P., Xiong, Q., Wu, S.C., Xia, L., Roy, S.S., Tolar, J., O'Connell, T.D., Kyba, M., et al. (2015). Derivation and high engraftment of patient-specific cardiomyocyte sheet using induced pluripotent stem cells generated from adult cardiac fibroblast. Circ. Heart Fail. *8*, 156–166.

Zhu, R., Millrod, M.A., Zambidis, E.T., and Tung, L. (2016). Variability of action potentials within and among cardiac cell clusters derived from human embryonic stem cells. Sci. Rep. *6*, 18544.